



Rain splash of dry sand revealed by high-speed imaging and sticky paper splash targets

David Jon Furbish,¹ Katherine K. Hamner,² Mark Schmeckle,³ Miriam N. Borosund,² and Simon Marius Mudd²

Received 13 March 2006; revised 22 June 2006; accepted 10 August 2006; published 16 January 2007.

[1] Rain splash transport of sediment on a sloping surface arises from a downslope drift of grains displaced ballistically by raindrop impacts. We use high-speed imaging of drop impacts on dry sand to describe the drop-to-grain momentum transfer as this varies with drop size and grain size and to clarify ingredients of downslope grain drift. The “splash” of many grains involves ejection of surface grains accelerated by grain-to-grain collisions ahead of the radially spreading front of a drop as it deforms into a saucer shape during impact. For a given sand size, splash distances are similar for different drop sizes, but the number of displaced grains increases with drop size in proportion to the momentum of the drop not infiltrated within the first millisecond of impact. We present a theoretical formulation for grain ejection which assumes that the proportion of ejected grains within any small azimuthal angular interval $d\theta$ about the center of impact is proportional to the momentum density of the spreading drop within $d\theta$ and that the momentum of ejected grains at angle θ is, on average, proportional to the momentum of the spreading drop at θ . This formulation, consistent with observed splash distances, suggests that downslope grain transport involves an asymmetry in both quantity and distance: more grains move downslope than upslope with increasing surface slope, and, on average, grains move farther downslope. This latter effect is primarily due to the radial variation in the surface-parallel momentum of the spreading drop. Surface-parallel transport increases approximately linearly with slope.

Citation: Furbish, D. J., K. K. Hamner, M. Schmeckle, M. N. Borosund, and S. M. Mudd (2007), Rain splash of dry sand revealed by high-speed imaging and sticky paper splash targets, *J. Geophys. Res.*, 112, F01001, doi:10.1029/2006JF000498.

1. Introduction

[2] Raindrops impacting a loose sediment surface can transfer part of their momentum to the sediment grains, whence the grains undergo “rain splash” that consists largely of grains being launched into arced trajectories away from drop impact sites. On a horizontal surface grains undergo directionally random displacements during a rain storm in the absence of wind; grain splash distances are determined by the details of the transfer of momentum between drops and grains. On an inclined surface grains collectively experience a net downslope drift in their motions; this downslope drift of grains represents rain splash transport, a process that has received considerable attention in hillslope geomorphology as well as in studies of erosional processes on agricultural lands [e.g., Ellison,

1944; DePloey and Savat, 1968; Carson and Kirkby, 1972; Mosley, 1973; Terry, 1998; van Dijk et al., 2002].

[3] Rain splash transport has been well documented by field measurements and under simulated rain and wind conditions [e.g., Moeyersons and DePloey, 1976; Kneale, 1982; Singer and Walker, 1983; Nearing and Bradford, 1985; Sharma et al., 1991; Erpul et al., 2002, 2003; Gabet and Dunne, 2003; van Dijk et al., 2003; Legout et al., 2005]. Whereas it is accepted that rain splash transport increases with land surface slope, perhaps nonlinearly [Moeyersons and DePloey, 1976], little is known about the details of the transfer of momentum from drops to grains that contribute to this downslope drift of grains. Herein we describe this momentum transfer process as revealed by high-speed imaging of drop impacts on sand targets under controlled laboratory conditions. We also describe details of grain splash distances obtained from sticky paper surrounding target drop impact sites. These techniques allow us to (1) clarify details of the drop-to-grain momentum transfer; (2) clarify the effects of varying drop size and grain size on the effectiveness of grain splash, and (3) clarify the ingredients of downslope grain drift in relation to surface slope. The work described here is focused on dry sand, although we preview results of initial experiments involving moist sand.

¹Department of Earth and Environmental Sciences and Department of Civil and Environmental Engineering, Vanderbilt University, Nashville, Tennessee, USA.

²Department of Earth and Environmental Sciences, Vanderbilt University, Nashville, Tennessee, USA.

³Department of Geography, Arizona State University, Tempe, Arizona, USA.

[4] The results of our experiments suggest that the “splash” of many grains involves ejection of those surface grains that are accelerated by grain-to-grain collisions ahead of the radially spreading front of a drop as it deforms into a saucer shape during impact. Under dry conditions, grains that become entrained in the spreading fluid front either do not detach from it, or are ejected as wetted clumps of grains. For a given sand size, splash distances are similar for different drop sizes. The number of detached grains, however, markedly increases with increasing drop size. Downslope grain drift consists of two parts: (1) more grains move downslope than upslope with increasing surface slope; and (2) on average grains move farther downslope than upslope. A first-order description of how drop momentum becomes distributed during impact nicely predicts the observed downslope asymmetry in grain numbers and splash distances. The formulation suggests that surface-parallel rain splash transport increases approximately linearly with surface slope.

2. Experiments

[5] Our experiments involve releasing individual drops from a height of ~ 5 m onto sand targets (Figure 1). The drops are released from a syringe with a blunted needle, where the needle diameter determines the drop size. The drops fall through a PVC pipe, minimizing their lateral “drift” due to air currents. Drops of three sizes (diameter $D = 2$ mm, 3 mm and 4 mm) are released onto the target, which consists of a circular hole with diameter of 2.5 cm and depth of 2 cm drilled into a wooden block. The sand surface is flush with the top of the target hole. We use three grain sizes (fine, medium and coarse quartz sand; diameter $d = 0.18$ mm, 0.35 mm and 0.84 mm). The experiments involve both dry and moist sand conditions, although we focus here on dry conditions.

[6] We estimate that drop fall speeds W at impact are $W \approx 6.2$ m s $^{-1}$ ($D = 2$ mm), $W \approx 7.2$ m s $^{-1}$ ($D = 3$ mm) and $W \approx 7.6$ m s $^{-1}$ ($D = 4$ mm), or 95%, 89% and 86% of terminal speeds, respectively (Appendix A). The target thickness is equivalent to $24d$, $57d$ and $110d$ for the coarse, medium and fine sand, respectively. *Haff and Anderson [1993]* suggest that an aeolian grain with speed of 1 m s $^{-1}$ impacting a grain surface disturbs the grains to a depth of 7–8 grain diameters. We suspect that a similar disturbance of grains occurs with the impact of a water drop, perhaps to a depth of $\sim 10d$ or more, so any effect on the surface splash of grains related to propagation of this disturbance is not limited by the target thickness.

[7] To characterize splash distance and azimuthal angle relative to the drop impact position, we place sticky paper with ~ 2 cm diameter holes centered on the 2.5 cm sand target such that the sand surface and paper are flush. The paper traps the splashed sand when it lands. The paper is photographed, then grain positions are digitized for further calculations. To obtain high color contrast between the grains and white sticky paper, we lightly paint the grains. This involves spreading the grains as a sparse monolayer on dry paper, applying a mist of black spray paint on the grains, drying them, spreading the grains again, then repainting them. The drops did not always land in the center of the sand target; therefore those landing near the



Figure 1. Experimental setup showing inclined board with sand target (black), high-wattage lighting, high-speed camera (covered by towel), and computer image of target. Sand target has diameter of 2.5 cm and depth of ~ 2 cm; experiments with sticky paper involve placing the paper (~ 2 cm diameter holes) over the sand target such that the sand surface is flush with the paper surface.

edge of the target, where we suspected interference with the sticky paper, were omitted from the analysis. In digitizing grain positions, we used the drop impact center (rather than the target center) as the coordinate origin, so some variability in measured grain positions occurs with this procedure.

[8] We performed three sets of experiments. In the first set we used high-speed imaging (500 frames per second) to view details of the drop impacts and resulting grain trajectories for both dry and moist sand conditions, using horizontal and inclined targets. For the moist sand experiments we filled the target hole with sand, saturated it, then allowed it to drain. In addition, we released drops onto a porous stone (at less than terminal velocity) to view how the drops partially infiltrated into the stone during impact. Over the course of the experiments we used two digital monochromatic cameras (Redlake MotionPro; DRS Technologies, Lightning RDT/1).

[9] A second set of experiments involved horizontal sticky paper targets, and all three drop and grain sizes. For each combination of drop and grain size, we applied from two to 10 drops for a total of 37 drops (Table 1). A third set of experiments involved 3 mm drops applied to sticky paper targets with medium sand inclined at six angles

Table 1. Experimental Drop and Grain Sizes

D , mm	d , mm		
	0.18	0.35	0.84
2	5/0 ^{oa}	3/0°	-/0 ^{ob}
3	4/0°	6/0° 23/10° – 30°	3/0°
4	2/0°	4/0°	10/0°

^aNumber of drops/experimental slope.

^bFew or no grains moved.

(0°, 10°, 15°, 20°, 25° and 30°). For each target angle we applied four to six drops for a total of 29 drops (Table 1).

3. Splash Behavior During Impact

3.1. Water Penetration

[10] Within the first millisecond (or less) of a raindrop impact on a sediment, water may penetrate the sediment surface [Mihara, 1952]. High-speed imaging reveals that the relative drop-to-grain size ratio, $R_0 = D/d$, exerts a first-order influence on this behavior. In our experiments a small drop ($D = 2$ mm) falling at 95% of its terminal velocity onto coarse sand ($d = 0.84$ mm) mostly infiltrates without splash, with negligible transfer of its momentum laterally to grains. In contrast, a large drop ($D = 4$ mm) falling at 86% of its terminal velocity onto fine sand ($d = 0.18$ mm) rapidly deforms laterally, transferring significant momentum to surrounding grains.

[11] Imaging of drops landing on a high-permeability porous stone similarly reveals qualitatively that small (2 mm) drops lose a significant part of their mass to infiltration with minimal lateral spreading, whereas much of the mass of the large (4 mm) drops accelerates laterally with proportionally less infiltration. Because these drops were released from the same small height of ~ 1 m, they had similar impact speeds (~ 4 m s⁻¹, Appendix A).

[12] As the drop decelerates vertically during impact, a dynamic fluid pressure develops at the water-sand interface beneath the drop footprint. The magnitude of this dynamic pressure $P \sim (\frac{1}{2})\rho W^2$, where ρ is the water density and W is the fall speed at impact. In addition, the pressure P may be enhanced locally within the impact footprint by a transient water hammer effect associated with a shock wave initiated at impact [Ghadiri and Payne, 1981]. The pressure P is sustained for a small time interval of order $\tau \sim D/W$. (As a point of reference, $\tau \sim 3 \times 10^{-4}$ s, 4×10^{-4} s and 5×10^{-4} s for drops with $D = 2$ mm, 3 mm and 4 mm falling at their experimental impact speeds W .) Air within the pores beneath the water-sand interface is initially at ambient atmospheric pressure. During τ , therefore, a sharp vertical pressure gradient occurs within the near-surface sand. This gradient, in concert with a water front that rapidly moves downward into the uppermost pores, displaces pore air downward and outward at a rate limited only by the pneumatic diffusivity of the sand. The advancing water front, in turn, is driven by a pressure gradient that is set by the difference between P and the air pressure beneath, and by the penetration distance ξ . Assuming pore air is readily displaced, and neglecting possible effects of a shock wave (with estimated duration of 5×10^{-5} s [Ghadiri and Payne, 1981]), this gradient is of order $\Delta p \sim P/\xi \sim \rho W^2/2\xi$,

and the rate of advance is limited by drag between the water and grains.

[13] Assuming a Darcy-like behavior for the penetrating water, $d\xi/dt \sim (k/\mu\Phi)\Delta p$, where k is the permeability, μ is the dynamic viscosity and Φ is the porosity. Following Kozeny [1927], Carman [1937], Irmay [1958], and others [see Bear, 1988, pp. 165–167], on dimensional and physical grounds the relation of permeability to porosity is specified by $k = Ad^2\Phi^3/(1 - \Phi)^2$, where A is a constant. Then, $d\xi/dt \sim [Ad^2\Phi^2/\mu(1 - \Phi)^2](\rho W^2/2\xi)$, or

$$\xi \frac{d\xi}{dt} \sim \frac{Ad^2\Phi^2\rho W^2}{2\mu(1 - \Phi)^2}. \quad (1)$$

Integration leads to $\xi \sim [(Ad^2\Phi^2\rho W^2/\mu(1 - \Phi)^2)t]^{1/2}$. With $t = \tau \sim D/W$ this gives [Hamner, 2005]

$$\frac{\xi}{d} \sim \frac{\Phi}{1 - \Phi} \sqrt{\frac{A\rho DW}{\mu}}. \quad (2)$$

Thus, for a given porosity Φ , the ratio of penetration distance to grain size, ξ/d , increases as the square root of drop size D and fall speed W (which are correlated), inasmuch as these set the dynamic pressure P and impact duration τ . Note, however, that (2) can be rewritten as $\xi/D \sim [\Phi/(1 - \Phi)](A\rho Wd/\mu R_0)^{1/2}$, which illustrates that, for a given grain size, the penetration distance relative to drop size, ξ/D , decreases with increasing drop-to-grain size ratio R_0 (Table 2). With increasing R_0 , less of the drop is absorbed and proportionally more drop mass is accelerated laterally. Conversely, with small R_0 , much of the drop is absorbed with minimal lateral motion, as revealed in the imaging. Typical parametric values suggest that the surface is wetted to only a few grain diameters at most (Table 2). We note that the assumption of Darcy-like behavior must be viewed as providing order-of-magnitude values of initial penetration given the high speeds involved (wherein fluid drag likely goes as the square of fluid speed), and given that effects related to deformation of the sand medium during τ are neglected.

[14] Returning to the drops landing on the porous stone, to order of magnitude, the volume of fluid infiltrating during τ is $V_I \sim \Phi\xi(\pi/4)D^2$ and the volume of a spherical drop is $V_D = (\pi/6)D^3$. The ratio $V_I/V_D \sim \Phi\xi(3\pi/2)/D \sim (3\pi/2)[\Phi^2/(1 - \Phi)](A\rho Wd/\mu R_0)^{1/2}$, which differs from the result above for ξ/D only by the factor $(3\pi/2)\Phi$. Thus, for constant d , Φ and W in these experiments, the proportion of mass lost to infiltration decreases with increasing drop size (and thus R_0), as suggested in the imaging.

3.2. Drop Deformation

[15] Images reveal that in some of the experiments an irregular high-angle corona-like splash of water occurs immediately after drop impact but before significant grain motions occur. This initial water splash is typically visible only in one frame, with residual droplet motions sometimes visible in a second frame, thus spanning ~ 0.002 s to 0.004 s. Thus $\tau \lesssim 0.002$ s. As a point of reference, our imaging of drops landing at low speed on a porous stone reveals their flattening behavior (see summary by Terry [1998]). The flattening of drops at higher speed, however, occurs within

Table 2. Measured and Estimated Drop and Sand Properties and Water Penetration Values

D , mm	d , mm	R_0	W , ^a m s ⁻¹	ξ/d ^b	ξ/D ^b	V_I/V_D ^b
2	0.18	11	6.2	1.1	0.096	0.14
2	0.35	5.7	6.2	1.1	0.19	0.26
2	0.84	2.4	6.2	1.1	0.45	0.63
3	0.18	17	7.2	1.4	0.085	0.12
3	0.35	8.6	7.2	1.4	0.16	0.23
3	0.84	3.6	7.2	1.4	0.39	0.56
4	0.18	22	7.6	1.7	0.075	0.11
4	0.35	11	7.6	1.7	0.15	0.21
4	0.84	4.8	7.6	1.7	0.35	0.50

^aFall speed W rounded to two significant digits.

^bAssumes porosity $\Phi = 0.30$ and permeability factor $A = 0.0005$.

the period of two successive frames, so 0.002 s or less, consistent with estimates of τ above. For sufficiently large R_0 , the drop flattens during impact into a saucer form and accelerates laterally. The central part of the drop experiences the dynamic pressure P with vertical deceleration. This drives the transfer of vertical fluid momentum to the lateral momentum of the spreading fluid saucer and its front. Unlike the deformation of a drop landing on a semirigid surface, which emits a high-angle rebound corona that is possibly associated with a transient shock wave [Ghadiri and Payne, 1981], our imaging reveals that the lateral motion of fluid spreading on dry sand is largely parallel to the surface. Although not readily visible in the images, one can envision that the spreading fluid, with thinning, experiences a loss of momentum at its base due to a combination of friction and grain entrainment [Terry, 1998], simultaneously wetting the surface to a depth of one or two grain diameters. With cessation of outward motion the drop and entrained grains form a small wetted grain “mat” that retracts inward due to surface tension.

[16] Drop deformation on an inclined surface is similar. The effect of the slope, however, is to produce a downslope bias in the lateral spreading of the drop associated with the downslope component of the incident impact velocity [Wright, 1986]. As in the experiments involving a horizontal target, small drops falling on coarse sand mostly infiltrate without splash.

[17] An approximate description of the geometry of the drop during impact (and spreading) obtains as follows. Just before impact a drop has fall velocity \mathbf{W} with slope-normal component $\mathbf{W}\cos\beta$ and downslope component $\mathbf{W}\sin\beta$, where β is the surface slope (Figure 2) [see also Wright, 1986]. Let \mathbf{v} denote a characteristic radial flow velocity. This surface-parallel velocity derives from a part \mathbf{v}_N related to the slope-normal component of \mathbf{W} and a part \mathbf{v}_S related to the downslope component of \mathbf{W} . That is, $\mathbf{v}_N = \alpha|\mathbf{W}|\cos\beta\mathbf{r}$ and $\mathbf{v}_S = \alpha|\mathbf{W}|\sin\beta\mathbf{s}$, where \mathbf{r} and \mathbf{s} are unit vectors in the radial and downslope directions, respectively, and α is a factor, assumed to be independent of β and \mathbf{W} , that characterizes the nonconservative transfer of vertical to surface-parallel momentum during impact [Wright, 1986]. This factor is on the order of 1/3 for drops falling on a thin water film [Allen, 1988] (see also data of Pietravalle et al. [2001]). The radial velocity \mathbf{v} is the vector, $\mathbf{v} = \mathbf{v}_N + \mathbf{v}_S$ (Figure 2). Let $V = |\mathbf{v}|/|\mathbf{v}_N|$ denote the magnitude of the radial velocity normalized by $|\mathbf{v}_N|$. Further, let θ denote the

angle about the center of impact, where $\theta = 0$ coincides with the downslope direction (Figure 2). Then the function $V(\theta)$ is (Appendix B)

$$V(\theta) = \Gamma \cos \theta + \sqrt{1 - \Gamma^2 \sin^2 \theta} \quad -\pi \leq \theta \leq \pi, \quad (3)$$

where $\Gamma = |\mathbf{v}_S|/|\mathbf{v}_N| \sim \tan\beta$. The function $V(\theta)$ provides a first-order description of how the magnitude of the drop momentum varies radially about the center of impact (Figure 2). Moreover, the probability density of V is (Appendix B)

$$f_{\Theta}(\theta) = \frac{\Gamma^2}{2\pi} (\cos^2 \theta - \sin^2 \theta) + \frac{\Gamma}{\pi} \cos \theta \sqrt{1 - \Gamma^2 \sin^2 \theta} + \frac{1}{2\pi} \quad -\pi \leq \theta \leq \pi. \quad (4)$$

The function $f_{\Theta}(\theta)$ provides a first-order description of how the drop momentum becomes distributed about the center of impact (Figure 3). For reference below the cumulative distribution function of $f_{\Theta}(\theta)$ is

$$F_{\Theta}(\theta) = \frac{\Gamma^2}{4\pi} \sin 2\theta + \frac{\Gamma}{2\pi} \sin \theta \sqrt{1 - \Gamma^2 \sin^2 \theta} + \frac{1}{2\pi} \sin^{-1}(\Gamma \sin \theta) + \frac{\theta}{2\pi} + \frac{1}{2} \quad -\pi \leq \theta \leq \pi. \quad (5)$$

In these functions Γ serves as a “concentration” factor. For $\Gamma = 0$, the functions V and f_{Θ} are uniformly distributed about the center of impact. With increasing Γ (i.e., with increasing slope), V and f_{Θ} become increasingly distributed downslope (Figures 2 and 3).

3.3. Grain Accelerations

[18] At the onset of lateral spreading of the drop, the spreading front begins to “push up” a small perimeter ridge of grains (Figure 4)[see also Huang et al., 1983]. This ridge propagates outward ahead of the advancing fluid front, and the “splash” of many grains involves ejection of those surface grains that are accelerated by grain-to-grain collisions within and ahead of this ridge. Imaging reveals that grain ejections mostly occur as drop expansion wanes. In

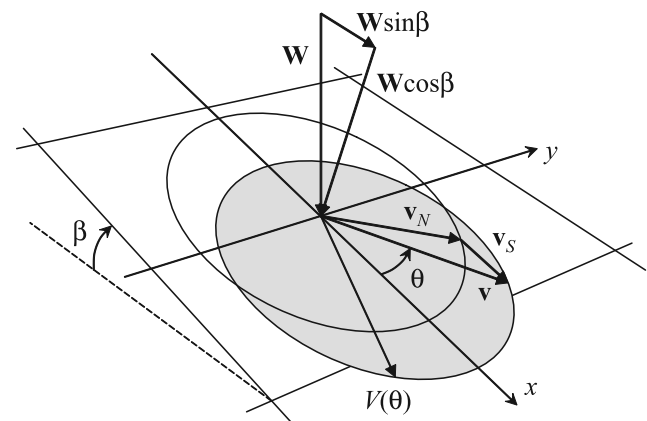


Figure 2. Definition diagram for vectors \mathbf{W} , \mathbf{v}_N , \mathbf{v}_S , and \mathbf{v} and dimensionless magnitude function $V(\theta)$.

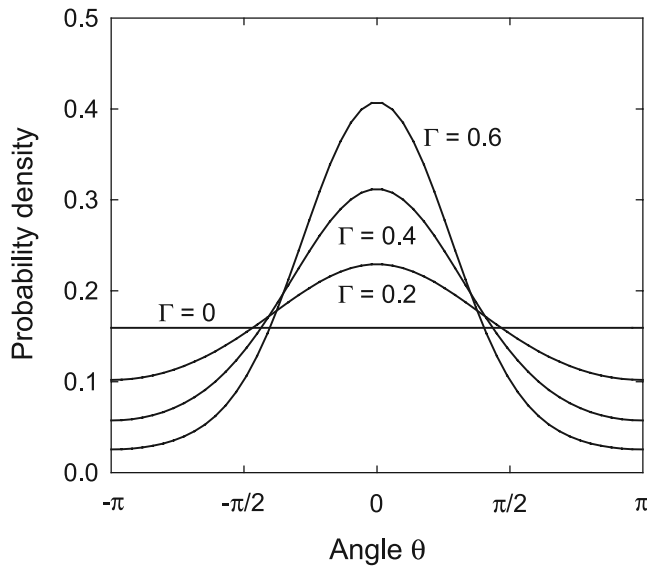


Figure 3. Plot of probability density $f_{\theta}(\theta)$ with varying concentration factor Γ ; downslope coincides with $\theta = 0$.

fact, initial inward retraction of the drop (as a wetted grain mat) by surface tension starts just as grains are being launched from the ridge.

[19] The ejected grains have mostly low-angle trajectories. Grains entrained within the spreading fluid either do not detach from it, or are ejected as wetted clumps of grains; this is particularly noticeable with large drops on fine sand (Figure 5). With collapse of the drop such that fluid motion is largely parallel to the sediment surface, the water surface is essentially flush with (or lower than) the sediment surface. This reflects the fact that during lateral expansion the drop entrains and transports surface grains outward from the center of the impact to form a small crater, as envisioned by *Al-Durrah and Bradford [1982]*. In addition, several of the videos reveal a small amount of surface dilation “far” ahead of the advancing fluid front (over a distance that is on the order of the radius of the impact footprint), suggesting grain-to-grain momentum transfer beneath the visible surface grains.

[20] The initial slope-parallel and slope-normal velocities of ejected grains appear to be highly correlated. Grains that are ejected from the top of the ridge (Figure 4 and Figure 6, $t = 0.004$ s to $t = 0.010$ s) have the highest initial speeds and highest launch angles relative to the surface. Grains that make up the middle and bottom parts of the ridge undergo significant grain-to-grain collisions, and thus have lower velocities and smaller launch angles. The combination of high-angle, high-velocity grains and low-angle, low-velocity grains leads to the distinctive inverted cone shape of the raindrop grain splash (Figure 5 and Figure 6, $t = 0.020$ s). Many more grains have low angles and low velocities than the relatively few high-speed grains ejected from the top of the ridge.

[21] For horizontal targets, ejected grain trajectories are statistically radially symmetrical. With increasing surface slope, this radial symmetry is replaced with increasingly asymmetric grain motions [*Carson and Kirkby, 1972, p. 189*]; at slopes approaching 30° , few upslope displace-

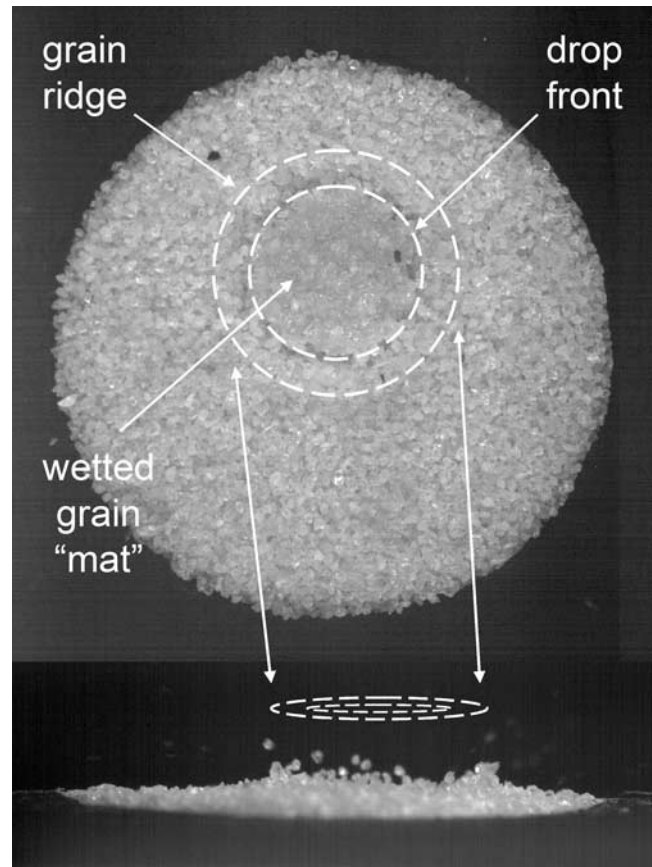


Figure 4. Image showing grains being ejected from a small grain ridge in front of a spreading drop front at approximately 0.004 s after initial impact; the ridge is advancing at a rate of ~ 25 cm s^{-1} .

ments occur. Imaging reveals a clear initial asymmetry in the speeds of the upslope and downslope parts of the grain ridge, and in the slope-parallel launch speeds of grains. Surface-normal launch speeds are similar on the upslope and downslope sides. As described below the slope-parallel



Figure 5. Image of splash from 4 mm drop on fine sand approximately 0.02 s after initial impact, showing ejected grains and grain clumps.

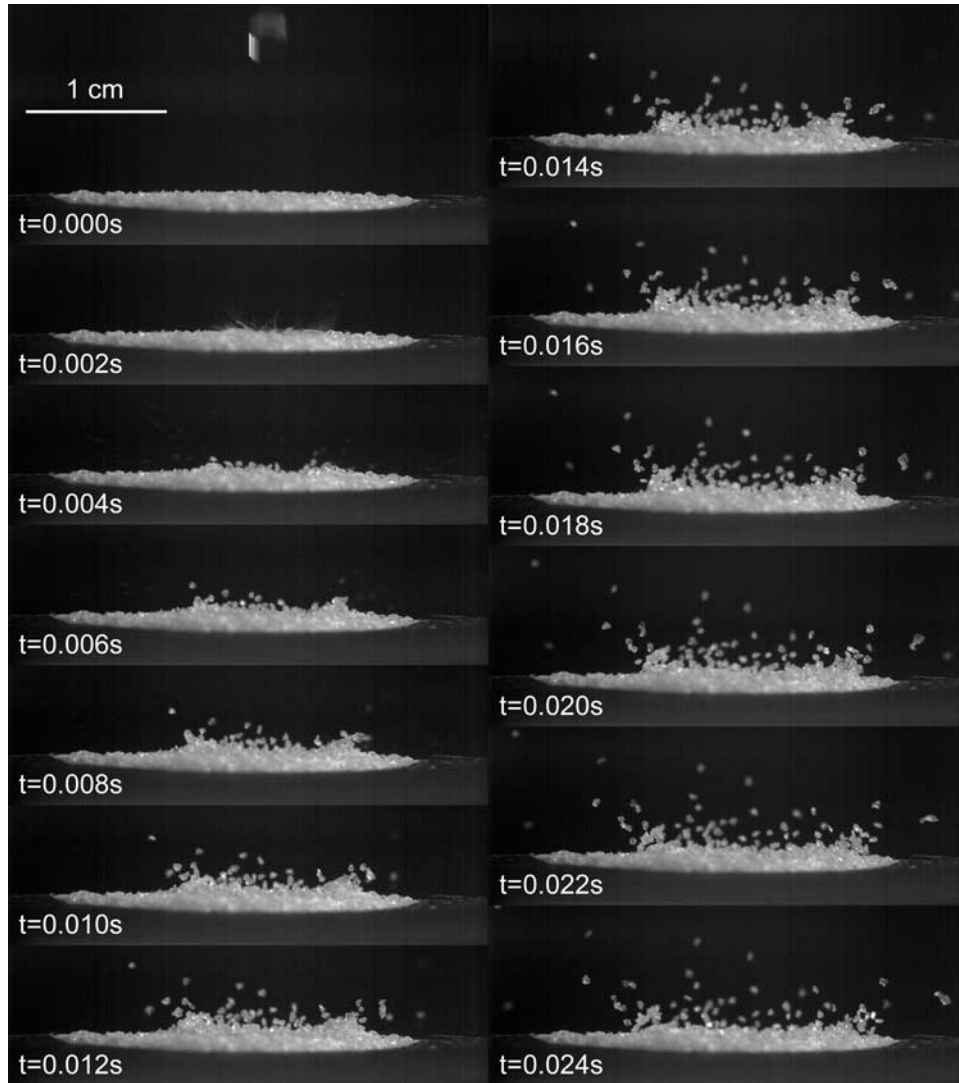


Figure 6. Time sequence image of grains ejected from grain ridge following drop impact, showing that grains ejected from top of ridge have highest initial speeds and launch angles, whereas grains that make up the middle and bottom part of ridge have lower initial speeds and launch angles following grain-to-grain collisions; note initial corona-like splash of water ($t = 0.002$ s) preceding significant grain motion.

asymmetry is manifest both in the distance that grains travel and in the numbers of grains.

4. Splash Patterns

4.1. Horizontal Targets

[22] For dry conditions and horizontal targets, radial splash distances are approximately exponentially distributed as postulated by *van Dijk et al.* [2002], but possibly with a heavy tail (Figure 7). The small proportion of grains landing in the 0–1 cm interval (measured from the center of impact) is partly due to censorship by the finite target size of 2 cm (thus grains landing within this interval are not accounted for), but is also partly due to the finite size of the drop-impact footprint (up to several drop diameters) over which grains are accelerated (also see discussion of the data of *Riezebos and Epema* [1985] by *van Dijk et al.* [2002]). In addition, the occurrence of grains in the 0–1 cm interval

(with the 2-cm target) reflects that the center of impact of some drops does not coincide with the target center.

[23] Following *van Dijk et al.* [2002] and others [*Wright*, 1987; *Mouzai and Bouhadef*, 2003; *Leguédouis et al.*, 2005; *Legout et al.*, 2005] the radial splash distance R is thus approximately distributed as

$$f_R(r) = \frac{1}{\mu_0} e^{-(r-r_0)/\mu_0} \quad r \geq r_0, \quad (6)$$

where r_0 is an exclusion distance and μ_0 is the average distance measured beyond r_0 . Here, r_0 may be interpreted as the radius of the drop-impact footprint.

[24] For a given sand size, splash distances are similar for different drop sizes; the average distance may increase only slightly with drop size (Figure 7). The number of ejected grains, however, markedly increases with increasing drop size (Figure 8). At the two extremes, 2 mm drops produce

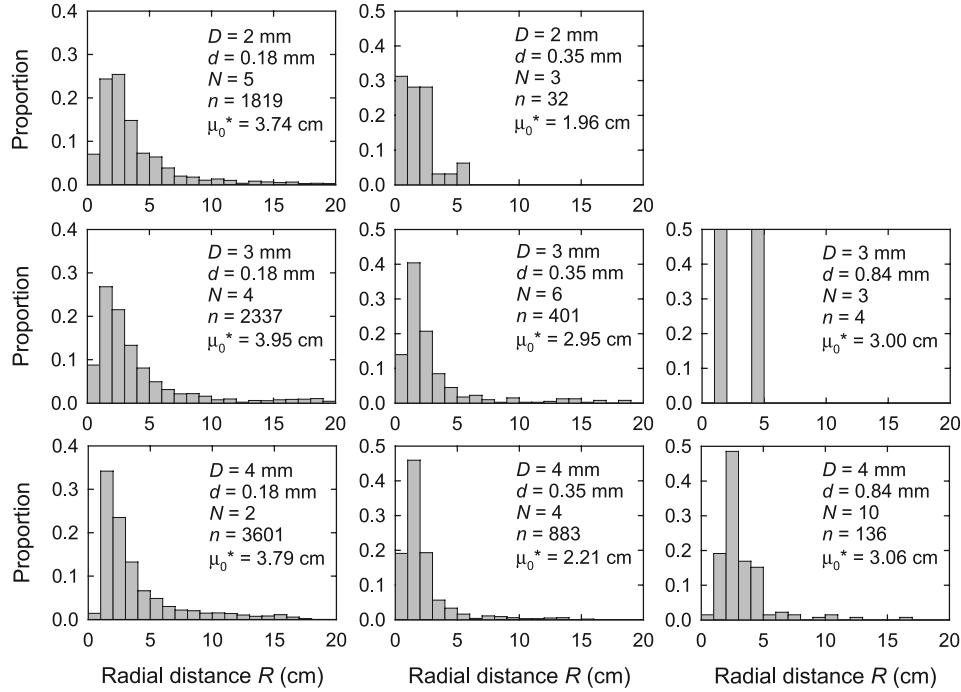


Figure 7. Histograms of radial splash distance R reflecting approximately exponential probability densities $f_R(r)$ with censorship in the 0–1 cm interval. Histograms are increasingly irregular for small total number of grains n collected over N drops and small drop-to-grain size ratio $D/d = R_0$; averages μ_0^* include all data (including $R \leq r_0$).

little or no movement of coarse sand, whereas 4 mm drops eject $\sim 1,800$ grains of fine sand per drop. *Mouzai and Bouhadef* [2003] similarly observe less than a 0.5 cm change in the average displacement distance for their largest four drop sizes ($D = 4.3$ cm to 5.8 cm) impacting sandy soil, although the total displaced mass increases sharply with drop size. The number of detached grains per drop is highly variable. Focusing on medium sand, the (observed) number of grains per drop varies from a low of 19 to a high of 116 across all 29 drops, but no systematic variation with slope exists (Figure 9). Pooling the data, the average number of detached grains per drop is 72; the standard deviation is 28.

[25] Inasmuch as grain motions are initiated by the surface-parallel momentum of the spreading drop, the total mass of ejected grains should be proportional to the area A_h “swept” by the spreading drop while possessing sufficient momentum. This is the area affected during the interval $\tau \sim D/W$ when the dynamic pressure P is present to drive lateral flow, and before the drop flattens to a critical thickness h where friction dominates and flow decelerates, then ceases; and A_h also depends on the excess volume of water $V_E = V_D - V_I$ not initially infiltrated during τ . If during τ the fluid saucer expands to volume $hA_h \sim V_E$ with characteristic momentum $hA_h|v_N| \sim V_E \alpha W$, then the total mass of ejected grains should be proportional to the “excess” momentum $V_E W$ (Figure 10 and Appendix C). Note in Figure 10 that (1) although the overall statistical fit does not significantly change between the plots of total ejected grain mass versus drop momentum $V_D W$, and grain mass versus excess momentum $V_E W$, the data generally collapse about a linear relation in the latter case and (2) the presence

of a “threshold” value of the momentum (~ 2 g cm s $^{-1}$) needed to initiate grain detachment. These results are consistent with the experiments of *Sharma et al.* [1991, Figures 1 and 2] and *Mouzai and Bouhadef* [2003, Figure 3] involving finer sediments (Appendix C).

4.2. Slope Effects

[26] We assume that to first order, the proportion of grains ejected within any small angular interval $d\theta$ is proportional to the momentum density of the spreading drop within $d\theta$. In this case the distribution of ejected grains (Figure 11) should mimic the probability density $f_\theta(\theta)$ as described by (4). Moreover, if $\theta = 0$ represents the downslope direction, the mean of the distribution of ejected grains should be centered at $\theta = 0$ and the concentration factor Γ should increase with slope. Data for dry medium sand compared with the cumulative distribution (5) confirm this point (Figure 12). Values of Γ estimated from these fits are consistent with the idea that $\Gamma \sim \tan\beta$ (Figure 13) wherein the slope of the line relating Γ to $\tan\beta$ is ~ 1 .

[27] We also assume that the momentum (mass and launch speed) of grains ejected at angle θ is on average proportional to the magnitude of the momentum of the spreading drop in the direction of θ . The average total grain mass ejected is independent of slope (Figure 9), suggesting that, to first order, the mean splash distance μ_0 in (6) for a horizontal surface is modulated by $V(\theta)$ in (3) (Appendix C). That is, the local mean $\mu(\theta)$ is

$$\mu(\theta) = \mu_0 \left(\Gamma \cos \theta + \sqrt{1 - \Gamma^2 \sin^2 \theta} \right) \quad -\pi \leq \theta \leq \pi. \quad (7)$$

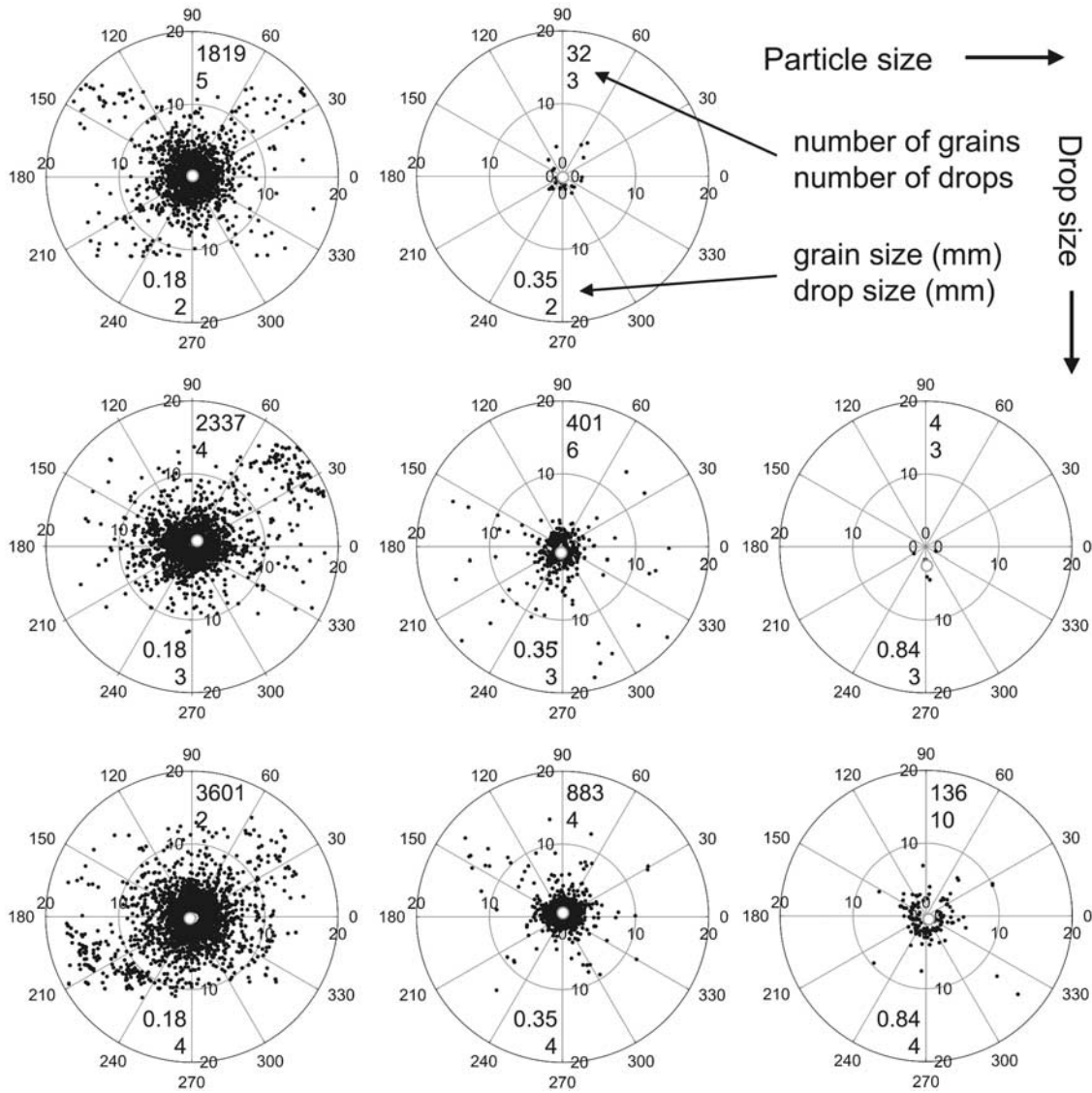


Figure 8. Radial plots of final ejected grain positions on horizontal surface showing symmetrical distributions, variations in numbers of splashed grains with drop size, and mass centroids (white circles). Radial distances are in cm.

With increasing Γ , downslope splash distances increase at the expense of upslope distances, depending locally on the angle θ . For $\Gamma = 0$, the local mean $\mu(\theta)$ reduces to the mean μ_0 associated with a horizontal surface, independent of θ . In effect (7) provides a momentum-based description of the “weighted average downslope splash length” of *van Dijk et al.* [2002].

[28] Combining (4), (6) and (7), the joint probability density of radial splash distance R and angle Θ is

$$f_{R\Theta}(r, \theta) = \frac{f_{\Theta}(\theta)}{\mu(\theta)} e^{-(r-r_0)/\mu(\theta)} \quad r \geq r_0 \quad -\pi \leq \theta \leq \pi, \quad (8)$$

which may be considered the product of the angular frequency of grain ejection, represented by $f_{\Theta}(\theta)$, and the radial magnitude of grain momentum (mass and splash

distance), represented by $[1/\mu(\theta)]\exp[-(r - r_0)/\mu(\theta)]$ (Figure 14). Note that $f_{R\Theta}(r, \theta)$ is a probability per unit length-angle (or specifically a probability per unit length per radian).

[29] Using $r = \sqrt{(x^2 + y^2)}$ with $r > r_0$, $r_0 = \sqrt{(x^2 + y^2)}$ with $|x, y| \leq r_0$, and $rdrd\theta = dx dy [1/\sqrt{(x^2 + y^2)}]$ obtained from the Jacobian of $[(\partial r/\partial x \ \partial r/\partial y)$ over $(\partial \theta/\partial x \ \partial \theta/\partial y)]$ with $x = r\cos\theta$ and $y = r\sin\theta$, we can transform (8) to its equivalent probability density in xy coordinates, $f_{XY}(x, y)$, a probability per unit area, then compute the slope-parallel marginal distribution of the splash distance X as

$$f_X(x) = \int_{-\infty}^{\infty} f_{XY}(x, y) dy. \quad (9)$$

Using measured values of μ_0 and Γ with $r_0 = 0.5$ cm for dry medium sand, numerical renditions of $f_X(x)$ reasonably

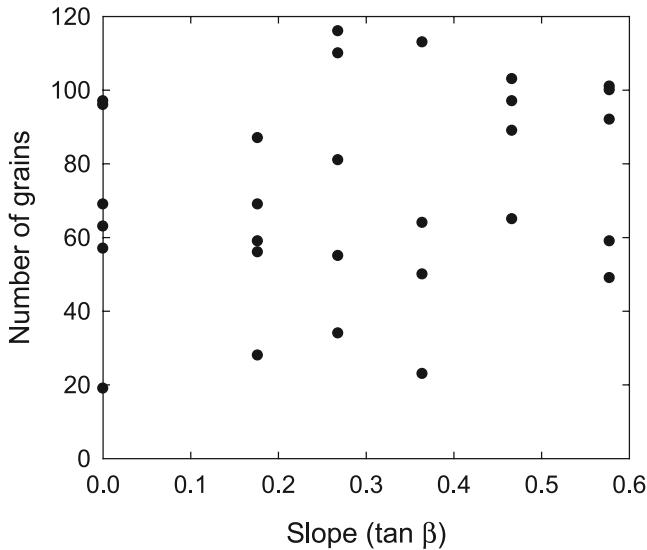


Figure 9. Plot of number of grains per drop versus target slope for 3 mm drops on medium sand.

mimic measured ones (Figure 15). In turn the average downslope displacement μ_X is

$$\mu_X = \int_{-\infty}^{\infty} xf_X(x)dx, \quad (10)$$

which we obtain numerically.

[30] Predictions of the average displacement μ_X , with one exception, systematically overestimate observed values from our experiments with medium dry sand on sloping targets (Figure 16), based on the measured average $\mu_0 = \mu_0^* - r_0 = 2.45$ for a horizontal target (Figure 6). Assuming that in the absence of target censorship the average $\mu_0 \approx 2$ cm based on an exponential fit to the data over the intervals 1–11 cm (Figure 6), predicted values of μ_X more closely match observed values (Figure 15). As described below the value of μ_X contributes to setting the overall rate of grain drift as a function of surface slope β . The value of μ_X , however, does not affect the form of this function.

5. Transport Rate and Surface Slope

[31] The average distance μ_X represents a downslope displacement in the center of mass of the grains activated during drop impact. The downslope flux of grains per unit length normal to the downslope direction is thus $q_N = N_a \mu_X$, where N_a [$L^{-2} t^{-1}$] is the number of grains activated (splashed) by raindrops per unit area per unit time. The activation density $N_a = N_D N_g$, where N_D [$L^{-2} t^{-1}$] is the number of drops per unit area per unit time and N_g is the average number of grains activated per drop. In turn, for vertical rainfall, $N_D = N_D^* \cos \beta$, where N_D^* is the number of drops per unit horizontal area per unit time. The grain flux q_N [$L^{-1} t^{-1}$] can be transformed to a volumetric flux [$L^2 t^{-1}$] or mass flux [$M L^{-1} t^{-1}$] upon multiplication by grain volume, or by grain volume and grain mass density, respectively. The drop rate density N_D [$L^{-2} t^{-1}$] can be related to rainfall intensity and drop size, and for a given

grain size the quantity N_g is related to drop size (and moisture conditions) as described above.

[32] In turn, the effect of surface slope on grain transport enters the formulation via the concentration factor $\Gamma \sim \tan \beta$, inasmuch as Γ modulates how, during impact, the momentum of a drop becomes distributed over the angle θ according to (4) and (7). This formulation otherwise contains only one parameter describing grain motions, the average radial splash distance on a horizontal surface, μ_0 . To view the effect of surface slope on transport, it is therefore convenient to form the ratio $\mu_\beta = \mu_X / \mu_0$. Numerical evaluations of (10) suggest that μ_β increases with surface slope as a weakly nonlinear function, although it is effectively linear up to $\sim 30^\circ$ ($\tan \beta = 0.58$) (Figure 17). Using this result we write $q_N = N_D N_g \mu_0 K_\beta \tan \beta$, where K_β is the (dimensionless) rate of increase in μ_β with $\tan \beta$ for given average radial distance μ_0 (Figure 17).

[33] Letting x' denote a horizontal coordinate axis that is positive in the downslope direction, the average displacement with respect to x' is $\mu_X \cos \beta$, so now $\mu_\beta = \mu_X \cos \beta / \mu_0$ increases with slope as a nonlinear function (Figure 17), and the grain flux parallel to x' is $\cos \beta N_D N_g \mu_0 K_\beta \tan \beta$. We may generalize this result to

$$\mathbf{q}_s = -K \cos(\tan^{-1} |\nabla \zeta|) \nabla \zeta. \quad (11)$$

Here $\mathbf{q}_s = \mathbf{i}q_{sx'} + \mathbf{j}q_{sy}$ [$L^2 t^{-1}$] is a volumetric flux per unit contour length with components $q_{sx'}$ and q_{sy} , $K = V_g N_D N_g \mu_0 K_\beta$ [$L^2 t^{-1}$] is a transport coefficient where $V_g = [L^3]$ is the individual grain volume, ζ is the local land surface elevation, and $\nabla = \mathbf{i}\partial/\partial x' + \mathbf{j}\partial/\partial y'$. As an example, for a rainfall intensity of 10 mm hr^{-1} involving 3 mm drops splashing on average 72 medium, dry sand grains per drop

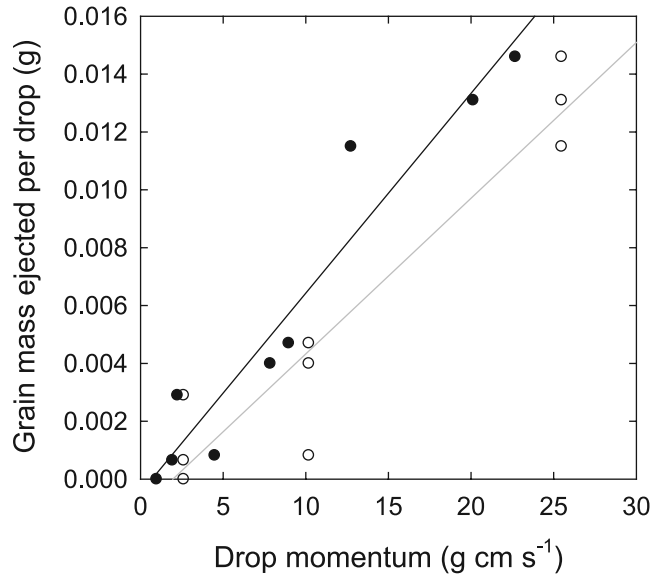


Figure 10. Plot of total grain mass ejected per drop versus drop momentum $\rho V_D W$ (open circles; fitted shaded line, $R^2 = 0.90$) and excess drop momentum $\rho V_E W$ (solid circles; fitted solid line, $R^2 = 0.93$) for data involving three drop sizes and three grain sizes on horizontal targets. Although overall statistical fit does not significantly change, data generally collapse about linear relation.

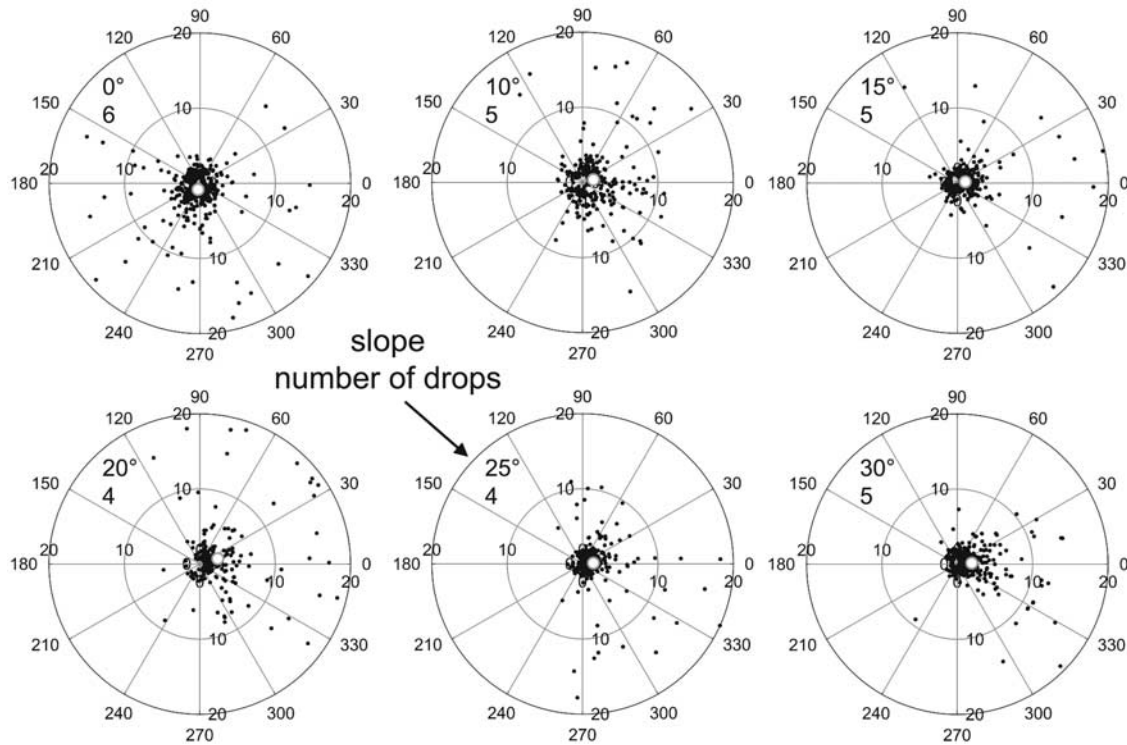


Figure 11. Radial plots of final ejected grain positions showing increasing asymmetry with increasing slope, with mass centroids (white circles). Radial distances are in cm.

with $\mu_0 = 2$ cm and $K_\beta \approx 1.74$, the coefficient $K \approx 0.0001$ $\text{cm}^{-2} \text{s}^{-1}$.

[34] Effects of raindrop properties (intensity, size distribution, kinetic energy) are examined further separately. We reemphasize that the work here is limited to dry sand conditions. Moreover, our experiments with sticky paper targets exclude the possibility that splashed grains might bounce upon landing, an effect we observed in experiments without sticky paper. We expect that such bouncing would increase average displacements, particularly with increasing slope.

6. Discussion and Conclusions

[35] It is well appreciated that grain detachment and splash generally increase with drop size in relation to drop momentum or kinetic energy. Nonetheless there is continuing debate regarding the relative performance of these and other quantities (for example, drop pressure and rain intensity) in predicting detachment [Salles *et al.*, 2001]. In seminal work on this topic, Sharma and Gupta [1989] and Sharma *et al.* [1991] plot and statistically fit detached grain mass versus both momentum and kinetic energy. They note that the fits (and R^2 values) are similar, and then state: “Since KE is predominantly used as an erosivity parameter in raindrop erosion modeling, our discussion henceforth will only consider KE-based relationships” [Sharma *et al.*, 1991, p. 305]. Indeed, the plots of detached grain mass versus momentum and grain mass versus kinetic energy for the loamy sand to clay soils reported by Sharma *et al.* [1991] suggest that linear fits between detached mass and momentum (involving a threshold momentum value) are at

least as good, if not better, than fits between detached mass and kinetic energy. Salles *et al.* [2001] point out that experimental splash data typically are not sufficiently precise to distinguish between these alternatives, and report that for both sand and silt loam, linear fits between detached grain mass and drop momentum, and between grain mass and kinetic energy, are not statistically different. Likewise, our data do not suggest a significant difference in linear fits between detached grain mass and momentum (Figure 10) and between grain mass and kinetic energy (not plotted), likely because the data span an insufficient range in drop momentum (or kinetic energy). Indeed, a simple scaling analysis (Appendix C) suggests that such plots ought to be nonlinear, as the slope of the physical relationship between ejected grain mass and either momentum or kinetic energy implicitly contains a characteristic (unmeasured) grain speed that varies with momentum or kinetic energy.

[36] Within this context, our imaging of drops landing on targets of different sizes of sand and on a high-permeability porous stone suggests that initial infiltration during impact [Mihara, 1952] modulates the relation between the mass of detached grains and drop size. Namely, for small drop-to-grain size ratio $R_0 = D/d$, significant infiltration can occur during impact due to the high dynamic pressure that momentarily exists during the small time interval $\tau \sim D/W$ (Table 2), such that the drop mass involved in lateral spreading is smaller than would otherwise occur. With large R_0 , the permeability of the sand limits infiltration during τ and proportionally more drop mass accelerates laterally. Inasmuch as the lateral momentum of the spreading drop is responsible for grain ejection, then the improved linear relation between the ejected grain mass and the momentum

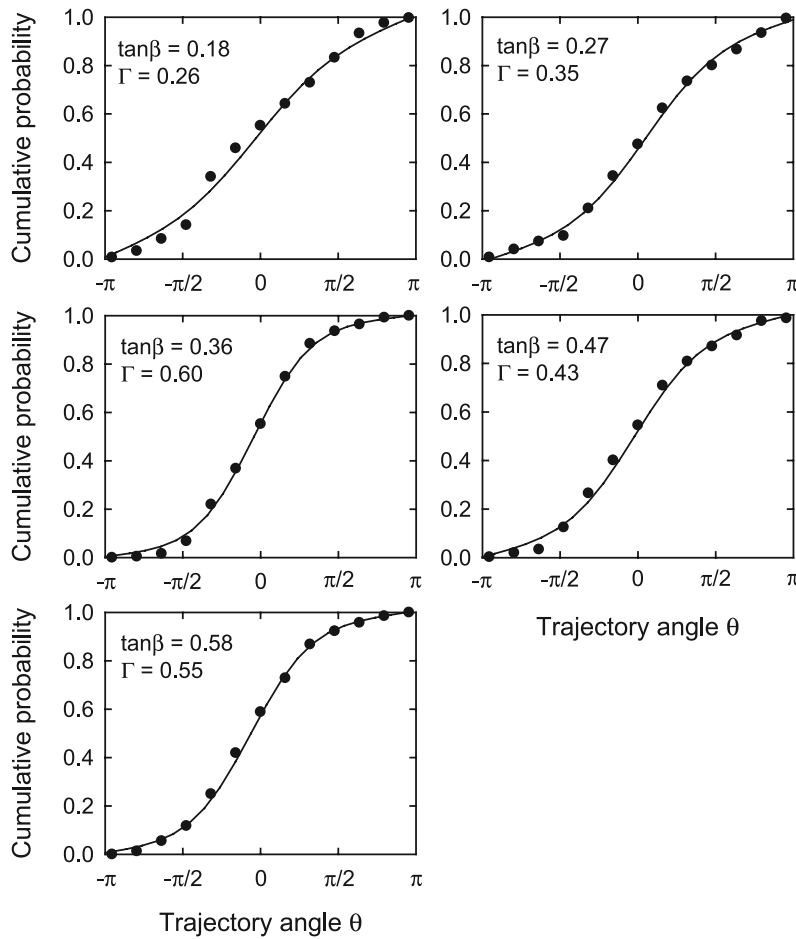


Figure 12. Plots of cumulative angular data (solid circles) with fitted theoretical cumulative probability functions (lines). Downslope corresponds with $\theta = 0$.

of the excess drop volume not infiltrated during τ , in comparison with the total drop momentum (Figure 10), is consistent with this point. Moreover, for small ratio R_0 an effect of infiltration is to contribute, in addition to effects of grain cohesion [Sharma and Gupta, 1989; Sharma et al., 1991], to the presence of a threshold momentum needed to initiate grain detachment.

[37] For horizontal targets the average radial splash distance μ_0^* may increase only slightly with drop size (and momentum) for a given grain size (Figure 7). Inasmuch as the total mass of ejected grains increases with drop momentum, then for an exponential (or any other) distribution of splash distances the number of grains displaced to all distances from the center of impact must also increase with drop momentum, although the proportions of grains at all distances remain similar [e.g., Mouzai and Bouhadef, 2003]. Thus, assuming that splash distances increase with grain speeds (Appendix D), the average distance μ_0^* is an insensitive measure of the partitioning of drop momentum into grain speed versus total grain mass for drops impacting a horizontal surface over the range of momentum encompassed in our experiments. We also note that target censorship, wherein the proportions of grains in the lowest intervals are underrepresented (Figure 7), may contribute to the absence of significant differences in the dependence of average splash distance on drop size. This censorship occurs because grains that are displaced, but not ejected out

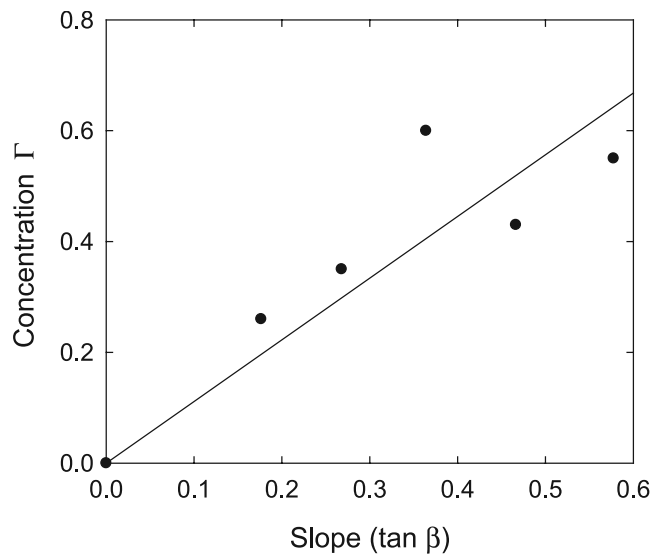


Figure 13. Plot of estimated values of concentration factor Γ versus surface slope ($\tan\beta$). Line has slope of 1.11 ($R^2 = 0.74$).

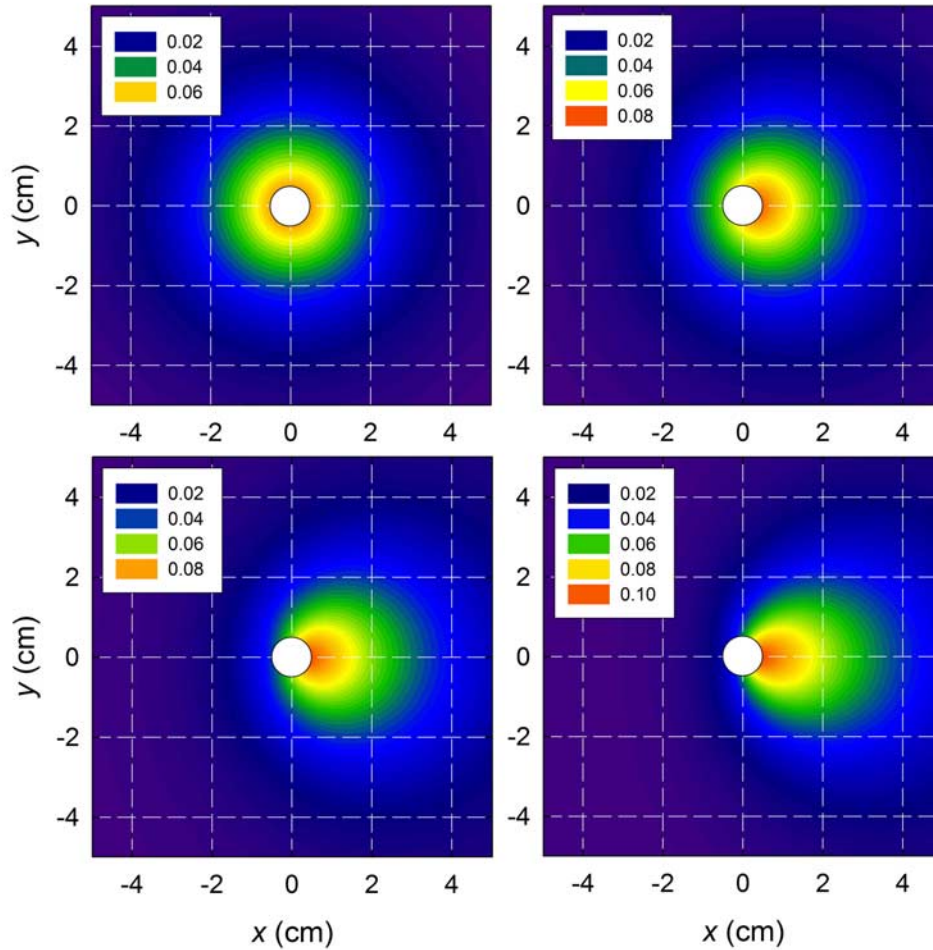


Figure 14. Contour plots of Cartesian transform of joint probability density $f_{R\Theta}(r, \theta)$ with concentration factor $\Gamma =$ (top left) 0, (top right) 0.2, (bottom left) 0.4, and (bottom right) 0.6 using exclusion distance $r_0 = 0.5$ (white circles) and $\mu_0 = 2.5$ cm. Downslope ($\theta = 0$) is to right.

of the target area onto the sticky paper, are not measured by our imaging techniques.

[38] Our imaging suggests that, following a corona-like fluid splash lasting less than 0.002 s, laterally accelerating water pushes up a small perimeter ridge of grains. This ridge propagates outward ahead of the advancing fluid front at speeds of less than 1 m s^{-1} , and the “splash” of many grains involves ejection of those surface grains that are accelerated by grain-to-grain collisions within and ahead of this ridge. The remnants of such ridges, moreover, are the rims of the familiar impact craters associated with raindrop imprints on granular material.

[39] The theoretical formulation for grain ejection assumes simply that, for a given drop size and grain size, the proportion of ejected grains within any small azimuthal angular interval $d\theta$ about the center of impact is proportional to the momentum density of the spreading drop within $d\theta$, and that the momentum (mass and launch speed) of ejected grains at angle θ is on average proportional to the magnitude of the momentum of the spreading drop at θ (Appendix C). Then, the resulting distribution of grains about the impact center in effect obtains as a frequency-magnitude product. This formulation therefore suggests that

the asymmetry contributing to downslope transport (drift) of grains consists of two parts. The first part involves quantity: more grains move downslope than upslope with increasing surface slope. The second part involves distance: on average grains move farther downslope than upslope. This is partly a geometrical effect due to asymmetry in the travel distances arising from the geometrical truncation of parabolic grain trajectories; but it is primarily due to the radial variation in the surface-parallel momentum of the spreading drop (Appendix D).

[40] The formulation suggests that the average downslope displacement of grains increases with surface slope as a weakly nonlinear function, although it is effectively linear up to $\sim 30^\circ$ (Figure 17). The average displacement measured with respect to a horizontal axis increases nonlinearly with surface slope by a factor involving the cosine of the slope (Figure 18). Our experiments with sticky paper targets, however, exclude the possibility that splashed grains in the experiments might bounce upon landing. We expect that such bouncing in nature would increase average displacements, particularly with increasing slope. Nonetheless, an attractive feature of the formulation is that, for a given drop size and grain size, grain motions are summarized by

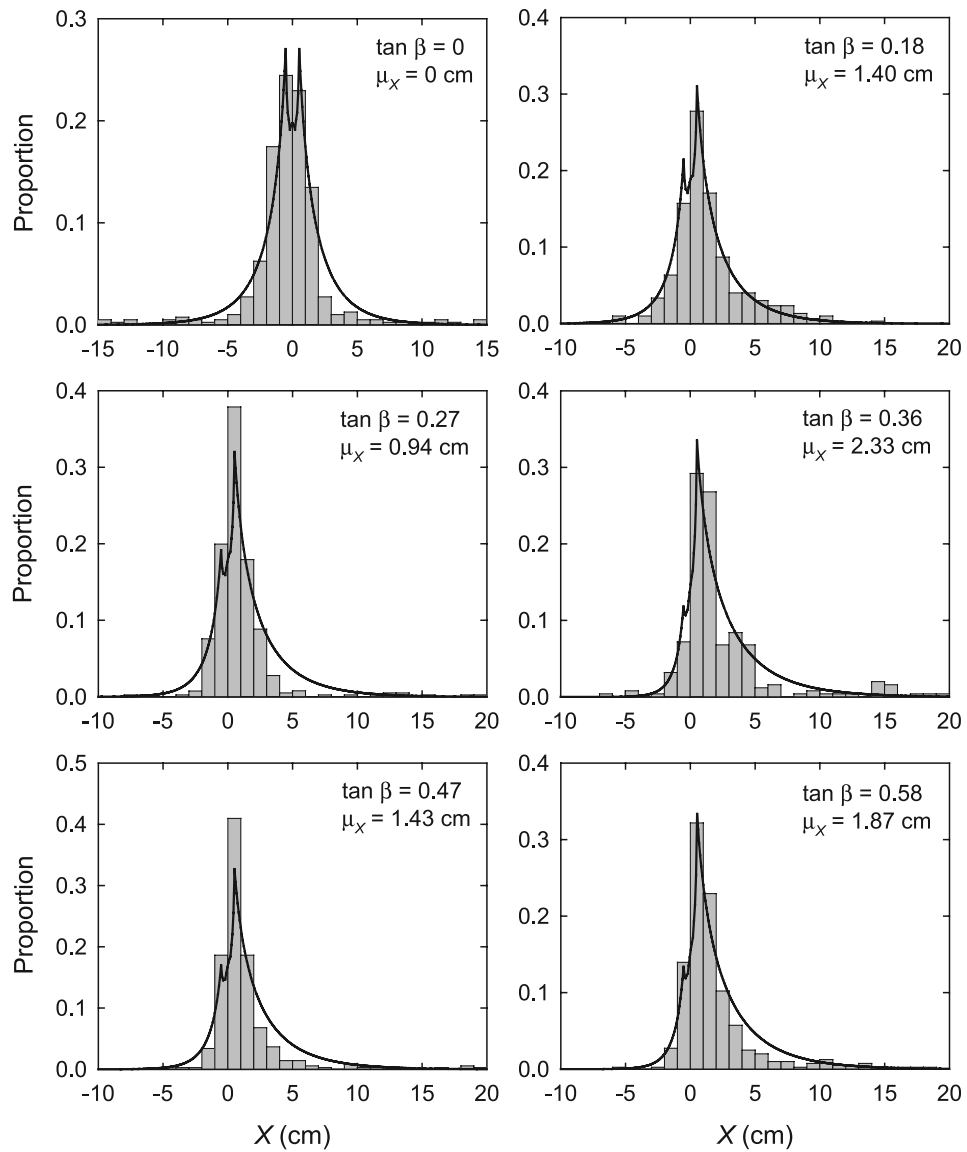


Figure 15. Measured histograms and simulated probability densities (lines) representing the marginal distribution $f_X(x)$ based on data for 3 mm drops on medium sand. Double peaks arise from the exclusion distance $r_0 = 0.5$ cm.

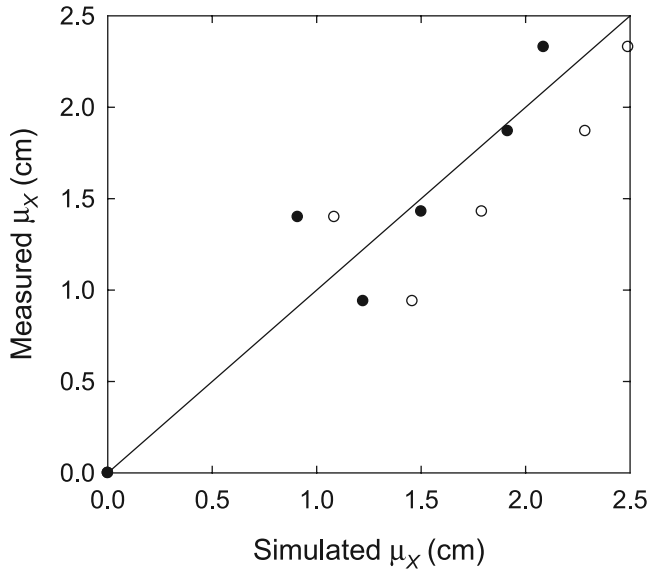


Figure 16. Plot of measured versus simulated average downslope distance μ_R assuming estimated values of the concentration factor Γ (Figure 9) and $r_0 = 0.5$ cm with $\mu_0 = 2.45$ cm (open circles) and $\mu_0 = 2$ cm (solid circles).

one key parameter, the average radial splash distance on a horizontal surface, μ_0 . The effect of surface slope independently enters the formulation via the concentration factor $\Gamma \sim \tan\beta$. Moreover, drop size and intensity explicitly enter the problem via their effects on grain activation (i.e., the number of grains ejected per drop, N_g , and the number of drops per unit area per unit time, N_D), analogous to the “splash detachment rate” of *van Dijk et al.* [2002].

[41] We reiterate that our work here focuses on dry sand conditions. Whereas we anticipate that ingredients of the formulation will equally apply to moist sediment conditions,

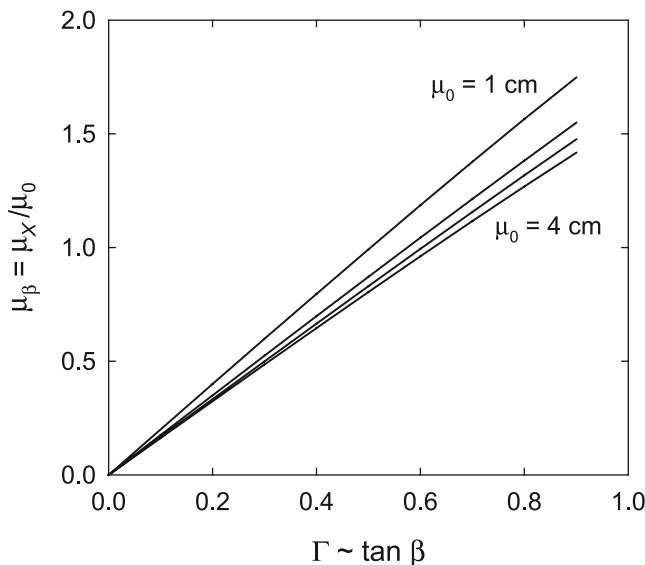


Figure 17. Plot of normalized average downslope displacement $\mu_\beta = \mu_X/\mu_0$ versus concentration factor Γ for $\mu_0 = 1$ cm, 2 cm, 3 cm, and 4 cm.

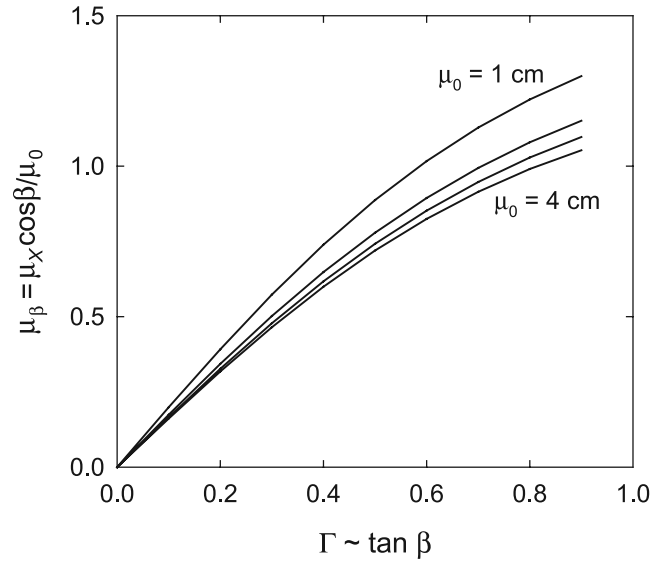


Figure 18. Plot of normalized average horizontal displacement $\mu_\beta = \mu_X \cos\beta/\mu_0$ versus concentration factor Γ for $\mu_0 = 1$ cm, 2 cm, 3 cm and 4 cm.

certain details (for example grain detachment numbers and splash distances) should be considered as applying to the behavior of sand transport early in a storm before the surface is significantly wetted, absent any effects of surface water ponding or flow [e.g., *Wan et al.*, 1996; *Terry*, 1998; *Goa et al.*, 2003], or effects of wind on drop and splash trajectories [e.g., *Moeyersons*, 1983; *de Lima*, 1989; *de Lima et al.*, 1993; *Wright*, 1986; *Erpul et al.*, 2002, 2003; *Warburton*, 2003].

Appendix A: Drop Fall Speed

[42] The motion of a spherical drop with density ρ and nominal diameter D falling with speed W in air with density ρ_a is given by

$$\frac{dW}{dt} = g - \frac{3\rho_a C_D}{4\rho D} W^2. \quad (\text{A1})$$

Here C_D is a coefficient of drag that varies only as a function of the Reynolds number, $Re = DW/\nu$ (Figure A1) [Edwards et al., 2001], where ν is the kinematic viscosity of air. Momentarily assuming that $C_D \approx \text{const}$ for fully turbulent conditions that ensue soon after the drop is released, then for $W = 0$ at $t = 0$, the solution of (A1) is

$$W = W_t \tanh\left(\sqrt{\frac{3\rho_a g C_D}{4\rho D}} t\right), \quad (\text{A2})$$

where the terminal fall speed W_t is

$$W_t = \sqrt{\frac{4\rho g D}{3\rho_a C_D}}. \quad (\text{A3})$$

[46] The probability density $f_{\Theta}(\theta)$ of $V(\theta)$ is obtained as follows. The small area dA_{θ} within a small azimuthal angle $d\theta$ is $dA_{\theta} = (1/2)V^2d\theta$. The total area A_{θ} from $-\pi$ to π is therefore

$$A_{\theta} = \int_0^{\pi} V^2 d\theta, \quad (\text{B5})$$

which, because of the dimensionless form of V , gives $A_{\theta} = \pi$. The cumulative distribution function $F_{\Theta}(\theta)$ of $f_{\Theta}(\theta)$, starting from $\theta = -\pi$, is

$$F_{\Theta}(\theta) = \frac{1}{2\pi} \int_{-\pi}^{\theta} V^2 d\theta. \quad (\text{B6})$$

Substituting (B4) into (B6) and evaluating the integral gives (5) in the text. In turn, the probability density function $f_{\Theta}(\theta) = dF_{\Theta}/d\theta$, which gives (4) in the text.

Appendix C: Relating Ejected Grain Mass and Speed to Drop Momentum

[47] Consider Newton's second law applied to a mass m_s of grains ejected during impact:

$$m_s \frac{dv}{dt} = F. \quad (\text{C1})$$

Here, F is the force applied to the grains to accelerate them from rest and v is a characteristic grain speed. For the purpose of order-of-magnitude scaling, we rewrite (C1) as

$$m_s \Delta v \sim F \Delta t, \quad (\text{C2})$$

so that the right side is an impulse.

[48] The force F in (C2) is supplied by the lateral acceleration of the drop. Conservation of momentum for the spreading drop with horizontal radial coordinate r requires that

$$\frac{\partial u}{\partial t} + u \frac{\partial u}{\partial r} = -\frac{1}{\rho} \frac{\partial p}{\partial r} + F_r, \quad (\text{C3})$$

where u is the fluid speed parallel to r , and F_r denotes the resisting forces of friction and surface tension per unit mass. Fluid acceleration is driven by the pressure term in (C3), and therefore early in the spreading motion this must be the dominant term. This means that the (early) lateral drop acceleration can be scaled as $(1/\rho)P/D$, where $P \sim (1/2)\rho W^2$ is the dynamic pressure during impact. In turn we scale $F \sim (1/2)\rho V_E W^2/D$, where ρV_E is the excess drop mass. The interval Δt scales with the duration of the impact. That is, $\Delta t \sim \tau \sim D/W$. Substituting these expressions into (C2) then gives

$$m_s \Delta v \sim \frac{\gamma}{2} \rho V_E W \quad (\text{C4})$$

where γ is a dimensionless coefficient that characterizes the nonconservative transfer of momentum from drop to grains. Inasmuch as the change in speed Δv is approximately constant, (C4) suggests that the mass of ejected

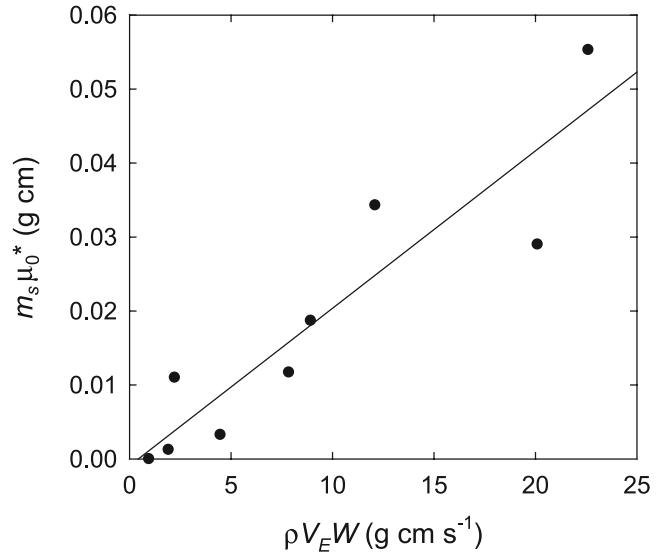


Figure C1. Plot of product of total grain mass ejected per drop m_s and average grain displacement μ_0^* versus excess drop momentum $\rho V_E W$ for data involving three drop sizes and three grain sizes on horizontal targets; compare with Figure 10.

grains m_s is proportional to the excess drop momentum $\rho V_E W$ (Figure 10).

[49] We now assume that Δv scales as $\mu_0^*/\delta t$, where μ_0^* is the average (radial) grain displacement for a horizontal surface, and δt is a short unspecified interval. Thus

$$m_s \mu_0^* \sim \frac{\gamma \delta t}{2} \rho V_E W. \quad (\text{C5})$$

Plotting $m_s \mu_0^*$ versus $\rho V_E W$ (Figure C1), the slope of the fitted line is $0.002 \sim \gamma \delta t/2$, suggesting that $\gamma \delta t \sim \text{O}[0.001 \text{ s}]$. For the experiments, $\tau \sim \Delta t \sim \text{O}[0.0001 \text{ s}]$ to 0.001 s , whereas grain motions mostly occur over an interval $\delta t \sim \text{O}[0.01 \text{ s}]$, suggesting that $\gamma \sim \text{O}[0.1]$. This is consistent with the idea that $\gamma \sim \alpha \sim \text{O}[0.1]$.

[50] Most of the variance in $m_s \mu_0^*$ (Figure C1) is associated with drop mass, ρV_E , because the drop speed, W , varies less than 20% (620 to 760 cm s^{-1}). According to (3), in contrast, in the downslope direction ($\theta = 0$) the dimensionless magnitude V increases by nearly 40% at a slope of $\beta = 20^\circ$, by nearly 60% at $\beta = 30^\circ$, and by 100% at $\beta = 45^\circ$. Moreover, according to (4), most of the surface-parallel momentum of the spreading drop is centered about the downslope direction. Inasmuch as this momentum accelerates surface grains in forming a perimeter ridge, then we assume part of this momentum is partitioned into the ridge speed and grain-to-grain collision speeds that set the local mean displacement $\mu(\theta) = \mu_0 V(\theta)$.

[51] To further clarify the significance of plots of ejected grain mass versus momentum, and grain mass versus kinetic energy (Figure 10) [e.g., *Sharma and Gupta*, 1989; *Sharma et al.*, 1991; *Mouzai and Bouhadef*, 2003], it is relevant to consider an hypothesis involving conservation of energy, in which case, analogous to (C4),

$$m_s v^2 \sim \gamma \rho V_E W^2. \quad (\text{C6})$$

A plot of ejected grain mass m_s versus kinetic energy $(1/2)\rho V_E W^2$ is thus like

$$m_s \sim \frac{\gamma}{v^2} \rho V_E W^2. \quad (C7)$$

If the characteristic grain speed v generally increases with the kinetic energy of the drop, then with $\gamma \sim \text{const}$ the slope of this relation, γ/v^2 , decreases with increasing kinetic energy, consistent with the characteristic convex upward form of the fitted lines reported by *Sharma et al.* [1991, Figures 1 and 2] and by *Mouzai and Bouhadef* [2003, Figure 3]. Alternatively, forming the ratio of grain mass to drop mass,

$$\frac{m_s}{\rho V_E} \sim \frac{\gamma}{v^2 \rho V_E} \rho V_E W^2. \quad (C8)$$

In a plot of $m_s/(\rho V_E)$ versus kinetic energy, according to (C8) the slope $\gamma/(v^2 \rho V_E)$ must decrease with increasing kinetic energy, and the rate of decrease should increase with drop mass, consistent with the results of *Sharma and Gupta* [1989, Figure 3]. Finally, rearranging (C4), a plot of ejected grain mass versus momentum is like

$$m_s \sim \frac{\gamma}{2\Delta v} \rho V_E W. \quad (C9)$$

Inasmuch as Δv increases with drop momentum, then over a sufficient range of momentum (and Δv) the slope of this relation, $\gamma/(2\Delta v)$, should decrease with increasing momentum [*Sharma and Gupta*, 1989, Figure 2b]. We suspect that our analogous plot (Figure 10) does not cover a sufficient range of momentum (and Δv) to display this change in slope. We also note that the coefficient γ may vary with drop momentum or kinetic energy.

Appendix D: Ballistic Trajectories and Transport

[52] The geometrical effect that surface slope has on grain splash distances, and the contribution to downslope transport due to asymmetry in these distances arising from the geometrical truncation of parabolic grain trajectories, can be described by the idealization of radially uniform grain trajectories (launch angles and speeds, and numbers of grains) about the drop impact. Consider a grain ejected from the surface with initial velocity magnitude v_0 at an angle φ relative to the surface with slope angle β . Let z momentarily denote the coordinate of a grain in a direction normal to the surface, and let r denote the radial coordinate of the grain in a direction that is parallel to the initial direction of its trajectory. Let θ denote the angle in the surface-parallel plane between the downslope direction ($\theta = 0$) and r . In this formulation we make the approximation that θ does not change during the trajectory of the grain, which is reasonable for $\varphi \lesssim 30^\circ$. The components g_r and g_z of the gravitational acceleration g acting on the grain are

$$g_r = g \sin \beta \cos \theta \quad \text{and} \quad g_z = -g \cos \beta. \quad (D1)$$

The ballistic equations in the r and z directions are then

$$r = v_0 \cos \varphi t + \frac{g}{2} \sin \beta \cos \theta t^2 \quad \text{and} \quad z = v_0 \sin \varphi t - \frac{g}{2} \cos \beta t^2. \quad (D2)$$

The z component in (D2) is satisfied for $z = 0$ when $t = 0$ and when $t = T$, the total grain travel time. Thus

$$T = \frac{2v_0 \sin \varphi}{g \cos \beta}. \quad (D3)$$

Letting $r = R$ when $t = T$, the r component in (D2) together with (D3) lead to

$$R = \frac{2v_0^2 \sin \varphi}{g \cos \beta} (\cos \varphi + \tan \beta \sin \varphi \cos \theta). \quad (D4)$$

Incorporating the exclusion distance r_0 , and assuming a radially uniform distribution of numbers of grain trajectories about the impact, the average downslope displacement is obtained as

$$\mu_X = \frac{1}{2\pi} \int_0^{2\pi} [r_0 \cos \theta + R(\theta) \cos \theta] d\theta = \frac{v_0^2 \sin \beta (1 - \cos^2 \varphi)}{g \cos^2 \beta}. \quad (D5)$$

Note that the exclusion distance r_0 factors out of this result. The average horizontal displacement $\mu_X \cos \beta$ is obtained by multiplying (D5) by $\cos \beta$, whence

$$\mu_X \cos \beta = \frac{v_0^2}{g} \tan \beta (1 - \cos^2 \varphi). \quad (D6)$$

[53] Measured from successive high-speed images, relatively large values of v_0 and φ for medium sand grains ejected during drop impact (Figure 6) are $v_0 \approx 45 \text{ cm s}^{-1}$ and $\varphi \approx 30^\circ$. Using (D6) these values give $\mu_X \cos \beta / \mu_0 \approx 0.2 \tan \beta$ with $\mu_0 \approx 3 \text{ cm}$, a relation that falls nearly an order of magnitude below the curves in Figure 18. Because most grains are ejected at smaller speeds and angles, actual values of the average displacement based on (10) are likely to be at least one, and possibly two, orders of magnitude larger than the average given by (D5). Thus downslope transport due to asymmetry in splash distances arising from the geometrical truncation of parabolic grain trajectories occurs, but is small. We also note that most grains are launched from the perimeter grain ridge at near zero φ . In this case the travel time T is independent of v_0 and depends only on the initial height on the ridge from which the grain is launched. In turn the displacement distant R is proportional to v_0 rather than v_0^2 .

[54] In addition to differences in (10) and (D5) that are due to the asymmetry of grain trajectories (both distances and numbers), the exclusion distance r_0 also plays an important role. With radial symmetry in the number of trajectories, r_0 does not figure into the average downslope displacement, (D5), as the proportion of grains displaced upslope and downslope is equal, and only differences in splash distances matter in determining μ_X . With radial asymmetry in the number of trajectories, in contrast, a higher proportion of grains is displaced downslope and, by definition, beyond the finite distance r_0 (Figure 14).

Notation

a, b, c velocity magnitude components [L t^{-1}].
 a_0, a_1, \dots empirical coefficients.

- A permeability factor.
 A_h area swept by spreading drop [L²].
 A_θ dimensionless area of $V(\theta)$.
 C_D coefficient of drag.
 d grain diameter [L].
 D drop diameter [L].
 $f_R(r)$ probability density function of radial splash distance R [L⁻¹].
 $f_X(x)$ slope-parallel marginal probability density function of splash distance X [L⁻¹].
 $f_{XY}(x,y)$ joint probability density function of splash distances X and Y [L⁻²].
 $f_\Theta(\theta)$ probability density of dimensionless velocity magnitude $V(\theta)$.
 $f_{R\Theta}(r,\theta)$ joint probability density function of splash distance R and trajectory angle Θ [L⁻¹].
 F force associated with spreading drop [M L t⁻²].
 F_r resisting force per unit mass associated with friction and surface tension [L t⁻²].
 $F_\Theta(\theta)$ cumulative distribution function of $f_\Theta(\theta)$.
 g acceleration due to gravity [L t⁻²].
 g_r, g_z components of g parallel to coordinate r and surface-normal coordinate z [L t⁻²].
 h critical drop thickness [L].
 \mathbf{i}, \mathbf{j} unit vectors in x' and y directions.
 k permeability [L²].
 K transport coefficient, $K = V_g N_D N_g \mu_0 K_\beta$ [L² t⁻¹].
 K_β rate of increase in dimensionless average splash distance μ_β with slope $\tan\beta$.
 m_s mass of ejected grains [M].
 N_a number of grains activated by raindrops per unit area per unit time [L⁻² t⁻¹].
 N_D number of drops per unit slope area per unit time, $N_D = N_D^* \cos\beta$ [L⁻² t⁻¹].
 N_D^* number of drops per unit horizontal area per unit time [L⁻² t⁻¹].
 N_g average number of grains activated per drop.
 $O[\]$ the term within the brackets indicates the order of magnitude of a quantity.
 p pressure [M L⁻¹ t⁻²].
 P dynamic pressure during drop impact, $P \sim (\frac{1}{2})\rho W^2$ [M L⁻¹ t⁻²].
 q_N grain flux [L⁻¹ t⁻¹].
 \mathbf{q}_s volumetric flux per unit contour length [L² t⁻¹].
 q_{sx}, q_{sy} components of flux \mathbf{q}_s [L² t⁻¹].
 r radial coordinate [L].
 \mathbf{r}, \mathbf{s} unit vectors in radial and downslope directions.
 r_0 radial exclusion distance [L].
 R radial splash distance [L].
 R_0 drop-to-grain size ratio, $R_0 = D/d$.
 t time [t].
 T total grain travel time [t].
 u fluid speed parallel to radial coordinate r [L t⁻¹].
 \mathbf{v}, v characteristic radial fluid velocity and its magnitude [L t⁻¹].
 v, v_0 grain speed and initial speed [L t⁻¹].
 \mathbf{v}_N, v_N surface-parallel radial fluid velocity and its magnitude related to slope-normal component of \mathbf{W} [L t⁻¹].
 \mathbf{v}_S, v_S surface-parallel fluid velocity and its magnitude related to downslope component of \mathbf{W} [L t⁻¹].
 $V(\theta)$ dimensionless velocity magnitude, $V = |\mathbf{v}|/|\mathbf{v}_M|$.
 V_D drop volume [L³].
 V_g individual grain volume.
 V_E excess drop volume, $V_E = V_D - V_I$ [L³].
 V_I volume of drop infiltrated during τ [L³].
 W_t terminal fall speed [L t⁻¹].
 \mathbf{W}, W drop fall velocity and its magnitude [L t⁻¹].
 x Cartesian coordinate parallel to downslope direction [L].
 x' horizontal Cartesian coordinate parallel to downslope direction [L].
 y horizontal Cartesian coordinate transverse to downslope direction [L].
 z vertical Cartesian coordinate, or surface-normal coordinate [L].
 z_p fall distance [L].
 α, γ factors characterizing nonconservative momentum transfer.
 β surface slope angle.
 Γ concentration factor, $\Gamma = |\mathbf{v}_S|/|\mathbf{v}_M|$.
 ζ land surface elevation [L].
 θ angular coordinate.
 Θ grain trajectory angle.
 μ water viscosity [M L⁻¹ t⁻¹].
 μ_0 average radial splash distance beyond r_0 for horizontal surface [L].
 μ_0^* measured average radial splash distance for horizontal surface [L].
 μ_X average downslope grain displacement [L].
 μ_β dimensionless ratio of average splash distances, $\mu_\beta = \mu_X/\mu_0$.
 $\mu(\theta)$ local average splash distance [L].
 ξ water penetration distance [L].
 ρ density of water [M L⁻³].
 ρ_a density of air [M L⁻³].
 τ small interval during impact, $\tau \sim D/W$ [t].
 ν kinematic viscosity of air [L² t⁻¹].
 φ grain launch angle relative to surface.
 Φ porosity.

[55] **Acknowledgments.** We appreciate the help of Chelsea Furbish and Amelia Furbish. Bob Anderson, Manny Gabet, Peter Haff, and Josh Roering provided critical reviews that helped us focus our ideas and presentation. This work was supported in part by the National Science Foundation (EAR-0405119).

References

- Al-Durrah, M. M., and J. M. Bradford (1982), The mechanism of raindrop splash on soil surfaces, *Soil Sci. Soc. Am. J.*, *46*, 1086–1090.
 Allen, R. F. (1988), The mechanics of splashing, *J. Colloid Interface Sci.*, *124*, 309–316.
 Bear, J. (1988), *Dynamics of Fluids in Porous Media*, Dover, Mineola, N. Y.
 Carman, P. C. (1937), Fluid flow through a granular bed, *Trans. Inst. Chem. Eng. London*, *15*, 150–156.
 Carson, M. A., and M. J. Kirkby (1972), *Hillslope Form and Process*, Cambridge Univ. Press, New York.
 de Lima, J. L. M. P. (1989), Raindrop splash anisotropy: Slope, wind and overland flow velocity effects, *Soil Technol.*, *2*, 71–78.
 de Lima, J. L. M. P., P. M. van Dijk, and W. P. Spaan (1993), Splash-saltation transport under wind driven rain, *Soil Technol.*, *5*, 151–166.
 DePloey, J., and J. Savat (1968), Contribution a l'etude de l'erosion par le splash, *Z. Geomorphol.*, *12*, 174–193.
 Edwards, B. F., J. W. Wilder, and E. E. Scime (2001), Dynamics of falling raindrops, *Eur. J. Phys.*, *22*, 113–118.
 Ellison, W. D. (1944), Studies of raindrop erosion, *Agric. Eng.*, *25*, 131–136.

- Erpul, G., L. D. Norton, and D. Gabriels (2002), Raindrop-induced and wind-driven soil particle transport, *Catena*, 47, 227–243.
- Erpul, G., L. D. Norton, and D. Gabriels (2003), Sediment transport from interrill areas under wind-driven rain, *J. Hydrol.*, 276, 184–197.
- Foote, G. B., and P. S. DuToit (1969), Terminal velocity of raindrops aloft, *J. Appl. Meteorol.*, 8, 249–253.
- Gabet, E. J., and T. Dunne (2003), Soil detachment by rain power, *Water Resour. Res.*, 39(1), 1002, doi:10.1029/2001WR000656.
- Gao, B., M. T. Walter, T. S. Stenhuis, J.-Y. Parlange, K. Nakano, C. W. Rose, and W. L. Hogarth (2003), Investigating ponding depth and soil detachability for a mechanistic erosion model using a simple experiment, *J. Hydrol.*, 277, 116–124.
- Ghadiri, H., and D. Payne (1981), Raindrop impact stress, *J. Soil Sci.*, 32, 41–48.
- Gunn, R., and G. D. Kinzer (1949), The terminal velocity of fall for water droplets in stagnant air, *J. Meteorol.*, 6, 243–248.
- Haff, P. K., and R. A. Anderson (1993), Grain scale simulations of loose sedimentary beds: The example of grain-bed impacts in aeolian saltation, *Sedimentology*, 40, 175–198.
- Hammer, K. K. (2005), The role of raindrop size and particle size in transport by rainsplash revealed by high-speed imaging, senior thesis, Vanderbilt Univ., Nashville, Tenn.
- Huang, C., J. M. Bradford, and J. M. Cushman (1983), A numerical study of raindrop impact phenomena: The elastic deformation case, *J. Soil Sci. Soc. Am.*, 47, 855–861.
- Irmay, S. (1958), On the theoretical derivation of Darcy and Forchheimer formulas, *Eos Trans. AGU*, 39, 702–707.
- Kneale, W. R. (1982), Field measurements of rainfall drop size distribution, and the relationship between rainfall parameters and soil movement by rainsplash, *Earth Surf. Processes Landforms*, 7, 499–502.
- Kozeny, J. (1927), Über kapillare Leitung des Wassers im Boden, *Sitzungsber. Akad. Wiss. Wien*, 136, 271–306.
- Legout, C., S. Leguëdois, Y. Le Bissonnais, and O. M. Issa (2005), Splash distance and size distributions for various soils, *Geoderma*, 124, 279–292, doi:10.1016/j.geoderma.2004.05.006.
- Leguëdois, S., O. Planchon, C. Legout, and Y. Le Bissonnais (2005), Splash projection distance for aggregated soils: Theory and experiment, *Soil Sci. Soc. Am. J.*, 69, 30–37.
- Mason, B. J. (1957), *The Physics of Clouds*, Oxford Univ. Press, New York.
- Mihara, Y. (1952), Raindrops and soil erosion, *Jpn. Natl. Inst. Agric. Sci. Bull.*, Engl. Transl., 1, 1–52.
- Moeyersons, J. (1983), Measurements of splash-saltation fluxes under oblique rain, *Catena Suppl.*, 4, 19–31.
- Moeyersons, J., and L. DePloey (1976), Quantitative data on splash erosion, simulated on unvegetated slopes, *Z. Geomorphol. Suppl.*, 25, 120–131.
- Mosley, M. P. (1973), Rainsplash and the convexity of badland divides, *Z. Geomorphol. Suppl.*, 18, 10–25.
- Mouzai, L., and M. Bouhadef (2003), Water drop erosivity: Effects on soil splash, *J. Hydraul. Res.*, 42, 61–68.
- Nearing, M. A., and J. M. Bradford (1985), Single waterdrop splash detachment and mechanical properties of soils, *Soil Sci. Soc. Am. J.*, 49, 547–552.
- Pietravalle, S., F. van den Bosch, S. J. Welham, S. R. Parker, and D. J. Lovell (2001), Modelling of rain splash trajectories and prediction of rain splash height, *Agric. For. Meteorol.*, 109, 171–185.
- Riezebos, H. T., and G. F. Epema (1985), Drop shape and erosivity. Part II. Splash detachment, transport and erosivity indices, *Earth Surf. Processes Landforms*, 10, 69–74.
- Salles, C., J. Poesen, and G. Govers (2001), A comparison of rain erosivity parameters for predicting soil detachment on interrills, in *Sustaining the Global Farm, 10th International Soil Conservation Organization Meeting, My 24–29, 1999*, edited by D. E. Stott, R. H. Mohtar, and G. C. Steinhardt, pp. 834–837, Natl. Soil Erosion Lab., West Lafayette, Indiana.
- Sharma, P. P., and S. C. Gupta (1989), Sand detachment by single raindrops of varying kinetic energy and momentum, *Soil Sci. Soc. Am. J.*, 53, 1005–1010.
- Sharma, P. P., S. C. Gupta, and W. J. Rawls (1991), Soil detachment by single raindrops of varying kinetic energy, *Soil Sci. Soc. Am. J.*, 55, 301–307.
- Singer, M. J., and P. H. Walker (1983), Rainfall runoff in soil erosion with simulated rainfall, overland flow and cover, *Aust. J. Soil Res.*, 21, 109–122.
- Terry, J. P. (1998), A rainsplash component analysis to define mechanisms of soil detachment and transportation, *Aust. J. Soil Sci.*, 36, 525–535.
- van Boxel, J. H. (1998), Numerical model for the fall speed of rain drops in a rain fall simulator, in *Proceedings of the International Workshop on Technical Aspects and Use of Wind Tunnels for Wind-Erosion Control: Combined Effects of Wind and Water Erosion on Processes, November 17–18 1997, Ghent, Belgium*, edited by D. Gabriels, and W. M. Cornelis, *ICE Spec. Rep. 1998/1*, pp. 77–85, Int. Cent. for Eremol., Univ. of Ghent, Ghent, Belgium.
- van Dijk, A. I. J. M., A. G. C. A. Meesters, and L. A. Bruijnzeel (2002), Exponential distribution theory and the interpretation of splash detachment and transport experiments, *Soil Sci. Soc. Am. J.*, 66, 1466–1474.
- van Dijk, A. I. J. M., L. A. Bruijnzeel, and S. E. Wiegman (2003), Measurements of rain splash on bench terraces in a humid tropical steep land environment, *Hydrol. Processes*, 17, 513–535.
- Wan, Y., S. A. El-Swaify, and R. A. Sutherland (1996), Partitioning interrill splash and wash dynamics: A novel laboratory approach, *Soil Technol.*, 9, 55–69.
- Warburton, J. (2003), Wind-splash erosion of bare peat on UK upland moorlands, *Catena*, 52, 191–207, doi:10.1016/S0341-8162(03)00014-6.
- Wright, A. C. (1986), A physically-based model of the dispersion of splash droplets ejected from a water drop impact, *Earth Surf. Processes Landforms*, 11, 351–367.
- Wright, A. C. (1987), A method of the redistribution of disaggregated soil particles by rainsplash, *Earth Surf. Processes Landforms*, 12, 583–596.

M. N. Borosund, D. J. Furbish, K. K. Hammer, and S. M. Mudd, Department of Earth and Environmental Sciences, Vanderbilt University, Nashville, TN 37235, USA. (david.j.furbish@vanderbilt.edu)
 M. Schmeeckle, Department of Geography, Arizona State University, Tempe, AZ 85287, USA.